SANDIA REPORT
SAND2022-xxxx
Printed September 2022

Sandia National Laboratories

Proton Tunable Analog Transistor for Low Power Computing

Donald A. Robinson, Michael E. Foster, Christopher H. Bennett, Austin Bhandarkar, Elliot J. Fuller, Vitalie Stavila, Catalin D. Spataru, Raga Krishnakumar, Neil Cole-Filipiak, Paul Schrader, Krupa Ramasesha, Mark D. Allendorf, and A. Alec Talin

Prepared by
Sandia National Laboratories
Albuquerque, New Mexico
87185 and Livermore,
California 94550

Issued by Sandia National Laboratories, operated for the United States Department of Energy by National Technology & Engineering Solutions of Sandia, LLC.

NOTICE: This report was prepared as an account of work sponsored by an agency of the United States Government. Neither the United States Government, nor any agency thereof, nor any of their employees, nor any of their contractors, subcontractors, or their employees, make any warranty, express or implied, or assume any legal liability or responsibility for the accuracy, completeness, or usefulness of any information, apparatus, product, or process disclosed, or represent that its use would not infringe privately owned rights. Reference herein to any specific commercial product, process, or service by trade name, trademark, manufacturer, or otherwise, does not necessarily constitute or imply its endorsement, recommendation, or favoring by the United States Government, any agency thereof, or any of their contractors or subcontractors. The views and opinions expressed herein do not necessarily state or reflect those of the United States Government, any agency thereof, or any of their contractors.

Printed in the United States of America. This report has been reproduced directly from the best available copy.

Available to DOE and DOE contractors from
U.S. Department of Energy
Office of Scientific and Technical Information
P.O. Box 62
Oak Ridge, TN 37831

Telephone: (865) 576-8401
Facsimile: (865) 576-5728
E-Mail: reports@osti.gov
Online ordering: http://www.osti.gov/scitech

Available to the public from
U.S. Department of Commerce
National Technical Information Service
5301 Shawnee Rd
Alexandria, VA 22312

Telephone: (800) 553-6847
Facsimile: (703) 605-6900
E-Mail: orders@ntis.gov
Online order: https://classic.ntis.gov/help/order-methods/

ABSTRACT

This project was broadly motivated by the need for new hardware that can process information such as images and sounds right at the point of where the information is sensed (e.g. edge computing). The project was further motivated by recent discoveries by group demonstrating that while certain organic polymer blends can be used to fabricate elements of such hardware, the need to mix ionic and electronic conducting phases imposed limits on performance, dimensional scalability and the degree of fundamental understanding of how such devices operated. As an alternative to blended polymers containing distinct ionic and electronic conducting phases, in this LDRD project we have discovered that a family of mixed valence coordination compounds called Prussian blue analogue (PBAs), with an open framework structure and ability to conduct both ionic and electronic charge, can be used for inkjet-printed flexible artificial synapses that reversibly switch conductance by more than four orders of magnitude based on electrochemically tunable oxidation state. Retention of programmed states is improved by nearly two orders of magnitude compared to the extensively studied organic polymers, thus enabling in-memory compute and avoiding energy costly off-chip access during training. We demonstrate dopamine detection using PBA synapses and biocompatibility with living neurons, evoking prospective application for brain-computer interfacing. By application of electron transfer theory to in-situ spectroscopic probing of intervalence charge transfer, we elucidate a switching mechanism whereby the degree of mixed valency between N-coordinated Ru sites controls the carrier concentration and mobility, as supported by density functional theory (DFT).

ACKNOWLEDGEMENTS

The authors would like to thank Matt Marinella for many valuable discussions.

CONTENTS

LIST OF FIGURES

This page left blank

ACRONYMS AND DEFINITIONS

Abbreviation	Definition
PBA	Prussian blue analog
DFT	Density functional theory
NVM	Non-volatile memory
ANN	Artificial neural network
ECRAM	Electrochemical random access memory
OECT	Organic electrochemical transistor
PEDOT:PSS	poly(3,4-ethylenedioxythiophene) doped with poly(styrene sulfonate)
MVC	Mixed valence compound
CT	Charge transfer
RuPBA	Ruthenium Prussian blue analog
fr-RuPBA	Fully reduced Ruthenium Prussian blue analog
pr-RuPBA	partially reduced Ruthenium Prussian blue analog
NN	Nearest neighbor
Ox	Oxidation
Re	Reduction
PEI	Polyethylene imine
OCR	Optical character recognition
MNIST	Modified National Institute of Standards
DA	Dopamine
UV-Vis-NIR	Ultraviolet-Visible-Near Infrared
MLCT	Metal to Ligand Charge Transfer
IVCT	Intervalence Charge Transfer
LiFSI	Lithium bis(fluorosulfonyl)imide
$Pyr_{14}TFSI$	N,N-Butylmethylpyrrolidinium bis(trifluoromethanesulfonyl)amide
as-RuPBA	as-synthesized Ruthenium Prussian blue analog
$IVCT_{CP}$	Cross-pore intervalence charge transfer
$IVCT_{NN}$	Nearest neighbor intervalence charge transfer
pDOS	Partial density of states
ITO	Indium tin oxide
XRD	X-ray diffraction
TEOS	tetraethylorthosilicate
DEMA:TfO	diethylmethylammonium trifluoromethanesulfonate
DMA	dimethylacetamide
PET	polyethylene teraphthalate

1. INTRODUCTION

Inspired by the in-memory computing architectures of biological systems, neuromorphic computing using crossbar arrays of artificial synapses based on non-volatile memory (NVM) devices with variable conductances has emerged as a new paradigm to enable massively parallel and ultra-low power computing hardware for data centric applications.[1-3] Although inference has been demonstrated successfully using crossbars based on a variety of NMV technologies, efficient learning and scaling to large arrays (>10^6 elements) remains a challenge due to the synaptic elements' non-ideal electrical characteristics which degrades artificial neural network (ANN) accuracy[4]. A further challenge is that in the conductive state memristors draw large currents >μA resulting in significant voltage drops in the interconnect wires and increased probability of failure in scaled arrays[5]. The organic polymer electrochemical random access memory (ECRAM) is an alternate approach that could solve many of these challenges, enabling both inference and parallel outer product updates, as recently demonstrated by Fuller et al.[3] An ECRAM consists of redox-active channel and gate electrodes in contact with a liquid or solid electrolyte. Ion insertion through the electrolyte controls the channel electronic conductivity, while electron transfer through an external circuit maintains overall charge neutrality. Unlike a rechargeable battery, in the ECRAM the voltage built-up across the electrolyte is kept to a minimum (typically <100 mV) by using the same material for the gate and channel. Elimination of the voltage offset simplifies integration of the ECRAM into programmable arrays by enabling the use of various selectors[3]. ECRAMs based on inorganic and organic materials have been recently demonstrated with conductance tuning occurring at potentials of just a few mV and hundreds to thousands of linearly and symmetrically programmable conductance states, enabling near ideal accuracy in neural network simulations.

Introduced in the 1980's, redox transistors with metallic gate electrodes and organic channel materials, also known as organic electrochemical transistors (OECTs), have been explored for a variety of applications such as chem- and bio-sensing, neural interfaces, and low cost printed circuits[6]. A typical channel material for OECTs is the conducting polymer poly(3,4-ethylenedioxythiophene) doped with poly(styrene sulfonate) (PEDOT:PSS). PEDOT is a p-type semiconducting polymer with mobile positively charged polarons that hop chain-to-chain.

Mixed valence compounds (MVCs) that accommodate facile ion insertion and extraction have recently garnered intense interest for applications beyond energy storage such as neuromorphic computing, thermal and magnetic switching, and electrocatalysis.[7] This interest is motivated by the possibility to tune the electronic structure of the host via the coupled ion/electron insertion/extraction reactions characteristic of electrochemical charge transfer (CT). Among the various classes of MVCs, the continually growing family of Prussian blue analog (PBA) coordination frameworks[8-10] stand out due to their high (electro)chemical stability,[11-13] fast ionic transport,[14, 15] biocompatibility and applications for biosensing,[16, 17] process compatibility with electron and photolithography,[18, 19] high electrocatalytic activity,[11, 12] and synthetic tunability.[9, 10] However, fundamental insight into the electronic conduction mechanism remains limited for most PBAs,[20, 21] including the archetypal PB,[22-25] thus hindering their utilization for electronics applications. This is surprising, given the success of electron transfer theory in explaining the electronic properties of many mixed valence coordination compounds,[26-28] including cyanide-bridged complexes that mimic the molecular building blocks of PBAs.[29-31]

In this report, we describe a Ru-based Prussian blue analogue[32] (RuPBA) as both a model system for understanding redox-tunable electronic delocalization in extended mixed valence coordination compounds[33, 34] and as an efficient active material for flexible electronic devices that rival organic electrochemical transistors (OECTs)[35, 36] for emerging analog memory[37-39] and

biointerfacing[40] applications. We elucidate the interrelationship between the electronic conductivity and the electrochemically tunable rate of intervalence CT using Marcus-Hush theory (MHT),[41, 42] Boltzmann transport theory, and operando absorption spectroscopy, indicating that hole mobility >1 $cm^2/(V \cdot s)$ is achievable in this material. Application of MHT to the absorption spectra at different oxidation states reveals that electronic conduction predominantly occurs through a cross-pore (*CP*) charge transfer pathway between N-coordinated Ru sites, as depicted in Fig. 1a, consistent with DFT predictions. To show the potential of RuPBA in neuromorphic computing, we demonstrate electrochemical random-access memory (ECRAM) artificial synapses[37, 43, 44] that switch conductance over a range of >4 orders of magnitude with a large linear regime, low read/write currents, strong endurance, and excellent long-term state retention. The RuPBA ECRAM is inkjet printed on flexible substrates, biocompatible, and sensitive to dopamine. To our knowledge, the RuPBA represents the first practical alternative material to polymer blend based OECTs, offering promising avenues for innovation via its distinct ion/electron conduction mechanism and large synthetic flexibility of the PBA family of compounds.

2. ELECTRONIC TRANSPORT AND ANALOG TUNING

Fig. 1a shows the idealized structure of RuPBA, depicted without $[Ru(CN)_6]^{4-}$ vacancies for simplicity, containing lithium ions intercalated within the square faces[45] of the cubic CN-bridged cages. The as-synthesized RuPBA contains 3 at.% of K^+ ions (Ru:K = 2.5:1), indicating that most of the Ru centers initially have a 2+ formal oxidation state. We expect the K^+ ions exchange with the Li^+ ions after the silica-based Li^+-containing ionogel electrolyte[46] layer is printed over the RuPBA layer. The transfer curve in Fig. 1c shows electrochemical tuning of the channel conductance from a lower limit of ~9×10^{-9} S to an upper limit of ~2×10^{-4} S. Based on the RuPBA film conductivity in the as deposited state (4×10^{-4} S/cm, Extended Data Fig. 1) and the measured conductance from Fig. 1c (2×10^{-5} S at V_{gd} = 0 V), the electrochemically tunable conductivity range extends from ca. 10^{-6} to 10^{-2} S/cm. Interestingly, the lower conductivity at the fully reduced RuPBA (*fr*-RuPBA) state (~10^{-6} S/cm) is close to that obtained by Xidis and Neff for *fr*-PB (5×10^{-7} S/cm).[24] We attribute the lower conductance limit at V_{gd} ~ 0.6 V to that of *fr*-RuPBA, where all Ru centers have a 2+ formal oxidation state and the structure contains the maximum amount of lithium ions. Partial oxidation of *fr*-RuPBA causes $Ru^{II/III}$ mixed valency and conductivity to increase.

Most of the accumulated electrochemical gating charge should be proportional to the amount of Ru^{II} species oxidized according to Faraday's law, and thus should also scale linearly with the charge carrier concentration. Analysis of the transfer data shows a voltage range where the conductance changes linearly with accumulated gate charge (see also Supplementary Information, Section S1). The trend suggests that only carrier concentration changes in the linear region, while mobility remains constant. Outside of this region, oxidation of the RuPBA channel either causes the mobility to increase (0.6 V $\lesssim V_{gd} \lesssim$ -0.1 V) or decrease (-0.3 V $\lesssim V_{gd} \lesssim$ -0.6 V). Upon oxidizing the channel further, the conductance decreases, indicating that a mixed valence form is the most conductive.

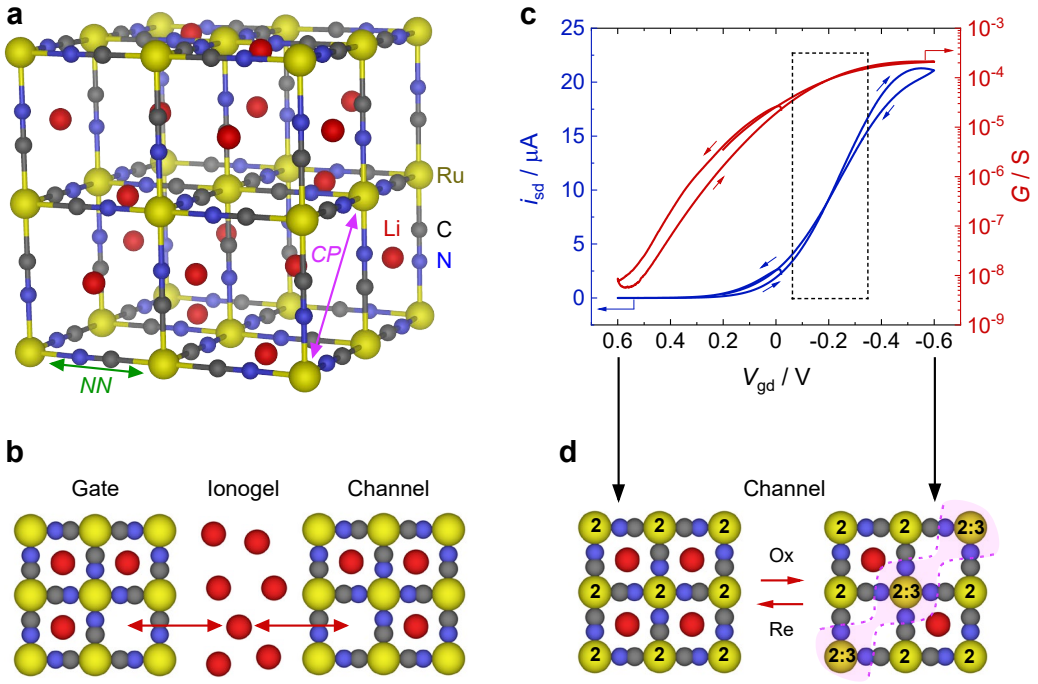

Fig. 1. Electrochemical doping of RuPBA. **a**, Idealized vacancy-free structure of partially lithiated RuPBA, $Li_3Ru_2[Ru(CN)_6]_2$, showing proposed cross-pore (*CP*) and nearest neighbor (*NN*) charge transfer paths. **b**, Schematic representing reversible Li^+ ion insertion into the RuPBA film at the gate and channel separated by a Li^+-containing ionogel electrolyte (See Supplementary Information, section S2, for a detailed description of the ECRAM device architecture). **c**, Transfer curve for a RuPBA/Li-ionogel device showing the resulting source-drain current of the channel (i_{sd}) on a linear scale (left y-axis, blue) and channel conductance on a logarithmic scale (G, right y-axis, red) when scanning the gate-drain voltage (V_{gd}) at 30 μV/s and applying a source-drain bias of 0.1 V. The dashed box designates the region where i_{sd} increases linearly as a function of electrochemical charge. **d**, Scheme conveying the change in Ru valency and degree of lithiation as the channel undergoes oxidation (Ox) and reduction (Re). Numeric labels on Ru atoms represent formal oxidation states and valence mixing. The region shown in pink highlights the proposed crosspore mixed valence conduction pathway, where electron delocalization occurs between neighboring N-coordinated Ru centers while C-coordinated Ru centers maintain localized 2+ formal oxidation states.

Consistent with the transfer characteristics (Fig. 1c), the voltage-controlled pulsed programming of an ECRAM device with a 0.75 ms 'write' pulse duration shows that the potentiation ($G\uparrow$) and depression ($G\downarrow$) ramps (Fig. 2a) are highly linear, which is desirable for high accuracy during training.[38, 39] Devices fabricated with a proton-conducting polymer-based ionogel electrolyte show better switching behavior in terms of linearity and symmetry, but switch more slowly, requiring more than 10-fold longer write pulse durations and twice as many pulses to cycle over a range of $G_{max} = 2G_{min}$ (Extended Data Fig. 3). The conductance range of 80-160 nS in Fig. 2a corresponds to a read current range of 8-16 nA at the applied read voltage (V_r = 0.1 V). The combination of low current and near-linear conductance tuning is ideal for energy-efficient programming.[38]

State retention is essential for nonvolatile synaptic memory. As shown in Fig. 2b, the programmed conductance over the entire range, 0.65-2.0 μS (G_{max} / G_{min} ~ 3), has a retention time of ~600 s (defined as $dG < 1$ %). The loss in retention at $G > G_0$ in Fig. 2b indicates that the more oxidized RuPBA states are less stable than the reduced states. However, the conductance remains stable within ±1% over a duration of ~10^4 s for the range below the initial state, 0.65-1.5 μS (G_{max}/G_{min} ~ 2), an improvement in comparison to the ~250 s retention time reported for PEDOT:PSS synapses programmed within a similar G_{max}/G_{min} range under inert environment.[47] PEDOT:PSS channels contain polyethyleneimine (PEI), which acts as an electron donor to annihilate electrochemically generated holes until the conductivity decays to its initial state. When charged to a lower conductivity, the PEI additive diffuses out of the channel and into the electrolyte, causing conductivity to increase over time towards the initial state.[47, 48] Given standard neural network training, the negative impacts of such volatility on network accuracy and energy efficiency might be considerable, *e.g.*, a deep neural network based on filamentary ReRAM where a ~5% conductance change over a period of 10^4 s at elevated temperature led to ~16 % loss in network accuracy, and could only be mitigated through a correction scheme applied every ~10^3 s.[49, 50] Yet, the conductance of RuPBA, when programmed at the lower range ($G < G_0$), does not trend back towards G_0 because RuPBA does not rely on a redox buffer such as PEI. This implies that, with only mild loss of analog range, non-volatile programming in the range of 0.65-1.5 μS can still enable efficient *in-situ* learning and retention for embedded biocompatible applications, with only minor alterations to normal training needed (*e.g.*, an array calibration step after each epoch to detect outlier weights exceeding some threshold above G_0, where they can be clipped/reset). As most neural network weights are low significance (low-conductance), the hardware mapping for this scheme is

natural and could lead to low overall error profiles at inference stage.[51] Meanwhile, the range clipping would not be a major detriment to learning performance, since a compressed range of 6-8 bits writable space is more than sufficient for most online learning applications using emerging non-volatile memory devices[52, 53] even when considering write noise in the loop.[54]

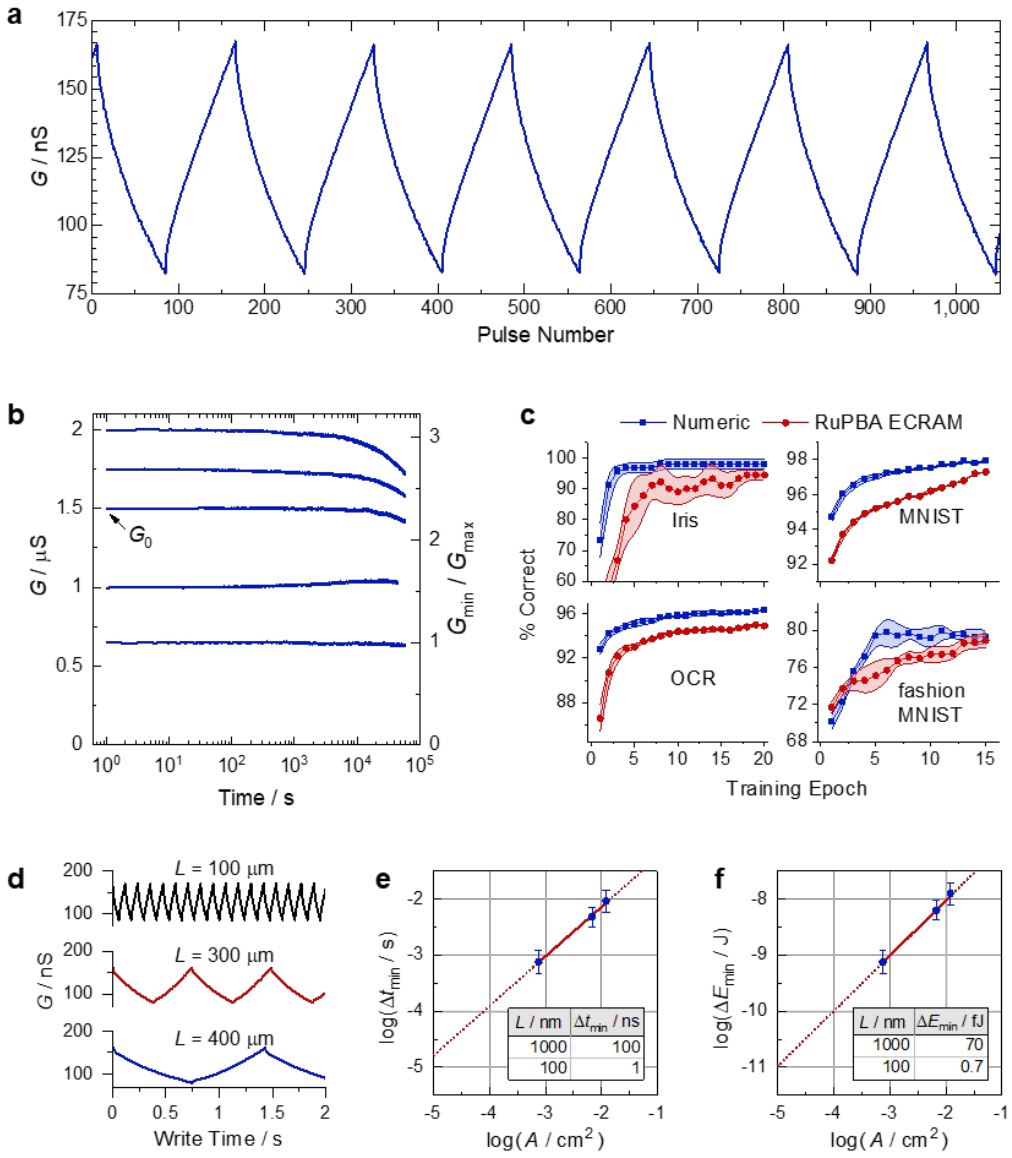

Fig. 2. Li-RuPBA ECRAM performance. **a**, Channel conductance during pulsed programming at V_{gd} = +1 V/-1 V for depression/potentiation at 0.75 ms gate pulse duration. **b**, Long term retention of 5 programmed conductance states. **c**, Simulated performance for neuromorphic tasks. Error bands represent standard deviation. **d**, Pulsed conductance programming with different channel dimensions, as labelled. 'Write Time' represents the total time that voltage is applied to the gate. Log-log plots showing relationship of channel area, A, to **e**, switching times, Δt_{min}, and **f**, switching energies, ΔE_{min}, required to change the channel conductance by an average value of ±1.0 nS. Inset tables show values obtained by extrapolation of the linear fits (red lines). The durations of the applied write pulses were 0.75 ms, 6 ms, and 10 ms in order of increasing area; this was done to achieve roughly equal numbers of conductance states per ramp, ~70 states for each of the three

devices. The channel length:width (L:W) aspect ratio of devices for parts **d**-**f** is 1:7.5, keeping the RuPBA film thickness constant at ~0.6 μm. Error bars represent the standard deviations for parts **e**-**f**. All measurements were performed under N_2 atmosphere at T = 300 K.

The channel conductance can be repeatedly cycled using 10^6 switching pulses without altering switching characteristics. From this data, we evaluate online learning by simulating a hardware multi-layer perceptron populated with RuBPA synapses. Due to the existence of a smooth, linear workable region optimal for on-chip backpropagation,[4] the RuBPA synapse generally performs excellently in the context of online learning. As shown in Fig 2c, on smaller tasks, such as the Iris flower classification problem[55] and the optical character recognition (OCR) task,[56, 57] RuPBA synapses achieve close agreement with ideal synapses (numerical). On larger neuromorphic tasks such as the fashion-MNIST[58] and MNIST task,[59] the gap between ideal and RuPBA devices diverges slightly more. Overall, our results are comparable to those of other leading linear and symmetric nonvolatile memory candidates.[37, 39, 43, 60-62]

The programming speed and energy efficiency of an ECRAM device depends on the electrochemical current of the 'write' step when a gate voltage is applied to change the redox state of the channel. Write currents should be minimized to reduce the energy cost.[37] However, higher faradaic write current densities should increase the ECRAM switching rate (faster charging). Fig. 2d shows conductance vs. write time traces for three devices with different channel areas, A, but a similar length:width aspect ratio (L:W = 1:7.5). The smallest device clearly operates more quickly, completing 12 potentiation/depression cycles before the larger device can finish the first cycle. The average times and energies required to switch the conductance by a magnitude of 1 nS are plotted versus channel area in Fig. 5e-f (See Supplementary Information, section S4). The smallest device achieves a switching time of 0.75 ms, comparable to the duration of action potentials in biological neurons.[63] The relationships are highly linear with log-log slopes of 1. From extrapolation, we predict that RuPBA ECRAM devices of similar architecture with 100 nm channel length should switch on the timescale of ~1 ns, much faster than biosynapses, with ~1 fJ write energy, a lower energy cost compared to ~10 fJ per synaptic event in biological synapses.[63] We anticipate that RuPBA devices fabricated with thinly layered channel/electrolyte/gate vertical architecture[43] would significantly lower the electrolytic gating resistance and increase the overall switching efficiency.[38]

RuPBA undergoes reduction upon reaction with dopamine (DA), an important neurotransmitter. Fig. 3a shows the design for a modified ECRAM device that allows DA to react with the RuPBA gate while preventing direct reaction with the channel. Fig. 3d shows that the device conductance decreases by ΔG when incrementally increasing the DA concentration, leading to the dose-response calibration curve. (see Supplementary Information, section S5, for a more detailed description of sensor operation). The RuPBA synapse achieves a 4 μM limit of detection, comparable to PEDOT:PSS-based OECTs.[40, 64]

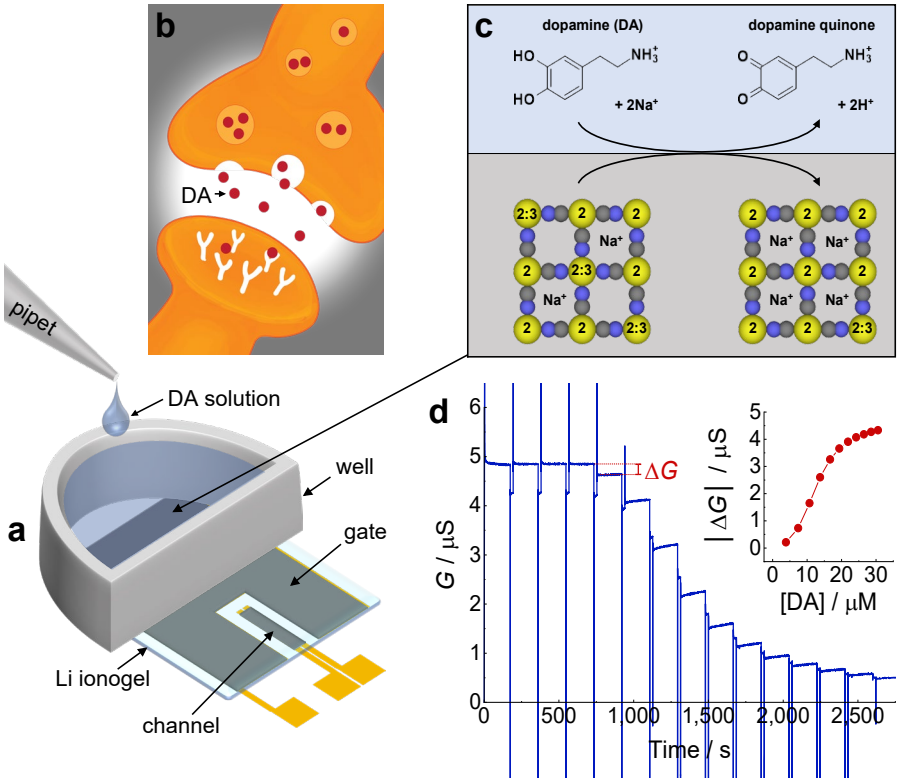

Fig. 3. Dopamine (DA) sensing with modified ECRAM cell. **a**, Sketch of modified device for dopamine sensing. **b**, Illustration of dopamine release from vesicles of a presynaptic neuron (top) to receptors of a postsynaptic neuron (bottom). **c**, Schematic of dopamine reaction with RuPBA in the portion of the device gate enclosed by the well. **d**, Conductance trace during incremental additions of dopamine and inset showing corresponding dose-response plot. In the inset, $|\Delta G| = |G - G_0|$, where G_0 (= 4.85 µS) is indicated by the topmost dashed horizontal red line on the conductance trace.

The sensitivity of RuPBA to dopamine establishes a basis to develop hybrid bio/artificial synapses.[40] For successful bio-interfacing, neuronal cells should be able to grow and thrive on RuPBA films. We find that cells seeded onto RuPBA films divide at a rate comparable to control cells, and that their viability is as high as control cells. Optical and scanning electron micrographs of the cells show interaction with and adherence to the RuPBA substrate. We conclude that RuPBA is nontoxic and non-refractory to cell growth. The compatibility of RuPBA with live neuronal cells signifies a promising first step towards utilizing electrochemical transistors to integrate biological and artificial analog neural networks.

In-situ UV-Vis-NIR spectroscopy provides a means to probe the electronic structure of RuPBA during electrochemical cycling. The film changes color from beige at the more reduced state to blue grey at the more oxidized state. Fig. 4a shows the evolution of absorption spectra as a RuPBA/ITO electrode is scanned from a fully reduced state at -0.2 V to a partially oxidized state at 1.0 V (versus Ag/AgCl wire). Following Behera et al., we assign the bands at ca. 30,000 cm^{-1} and 6000 cm^{-1} to the metal-to-ligand charge transfer (MLCT) and intervalence charge transfer (IVCT)

reactions, respectively.[32] As the film is oxidized, the MLCT intensity decreases while the IVCT intensity increases. Like the conductance vs gate voltage trend of Fig. 1c, the relationship of IVCT absorbance to electrode potential in Fig. 4b is sigmoidal and reversible. The absorbance vs potential response is consistent over multiple cycles in this 1.2 V potential window. Fig. 4c shows the interrelationship of applied gate voltage, IVCT absorbance, and conductance when switching conductance across four orders of magnitude in a RuPBA ECRAM device. The correlation of conductance to IVCT absorbance signifies that the electronic conductivity of RuPBA is inextricably linked to the rate of intervalence charge transfer.

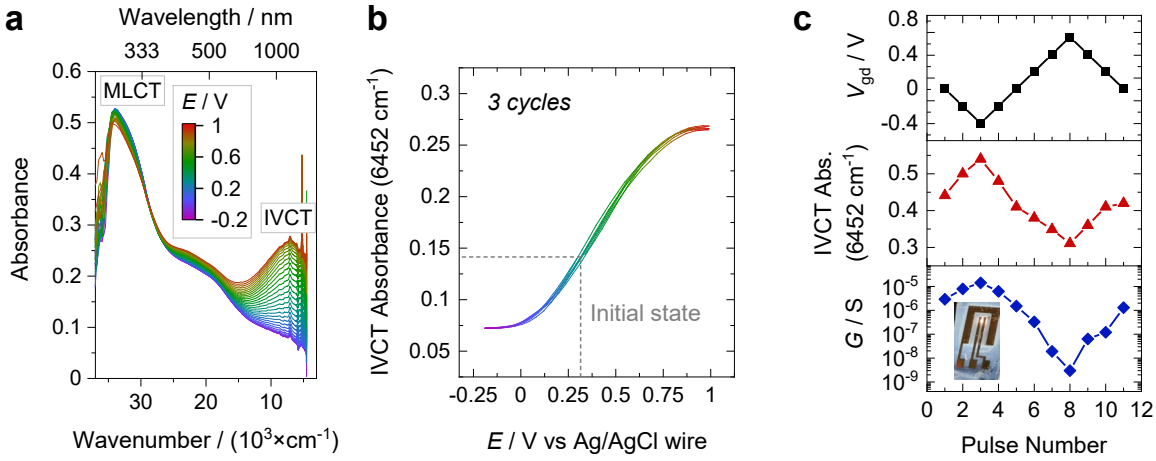

Fig. 4. In-situ UV-Vis-NIR absorption spectroscopy of RuPBA films during voltammetric cycling. **a-b**, Results from cyclic voltammetry of RuPBA film on indium tin oxide (ITO)-coated glass in contact with liquid electrolyte containing 1.0 M LiFSI dissolved in $Pyr_{14}TFSI$, scan rate of 50 μV/s. **a**, Overlaid spectra recorded as the potential, *E*, was scanned from -0.2 to 1.0 V (vs Ag/AgCl wire quasireference electrode). **b**, Absorbance monitored at 6452 cm^{-1}, as taken from the 2nd scan cycle, with the initially recorded open circuit potential at equilibrium, 'initial state', marked by the gray dashed lines. **c**, Measurements of the conductance and IVCT absorbance in the channel region of an ECRAM device after potentiostatic charging at varied gate voltages (V_{gd}). Conductance is shown on a logarithmic scale. Inset image on the conductance plot shows the optical path from the tungsten halogen light source through the device channel.

When extending the applied potential to 1.4 V, we observe an additional trend in the IVCT region of the UV-Vis-NIR spectra. The lowest energy maximum at ca. 6450 cm^{-1} follows the trend as discussed above from -0.2 to 1.0 V, but then decreases in absorbance from 1.0 to 1.4 V. The absorbance at ca. 13,000 cm^{-1}, however, continues to increase as RuPBA undergoes oxidation to 1.4 V. The two observed trends reveal that two distinct IVCT processes occur in RuPBA, and that the absorbance of the lower energy IVCT correlates with conductivity.

The strong correlation of IVCT absorbance with conductivity supports a mechanism whereby electronic transport in RuPBA occurs through adiabatic intramolecular CT reactions. As shown in Fig. 5a, deconvolution of the UV-Vis-NIR spectrum for a film of the as-synthesized RuPBA (*as*-RuPBA) suggests at least seven different overlapping optical absorption bands in the wavenumber (ν) range of 35,000 to 4,000 cm^{-1}, consistent with the previous report.[32] We assign the two lowest energy bands at ca. 8400 cm^{-1} (1.0 eV) and 5100 cm^{-1} (0.6 eV) to two different IVCT transitions, as depicted in Fig. 5a. The higher energy band ($IVCT_{NN}$) corresponds to electron transfer from N-

coordinated Ru (N-Ru) to its nearest neighbor, C-coordinated Ru (C-Ru), as separated by the cyanide bridge. The lower energy band ($IVCT_{CP}$) corresponds to 'cross-pore' transfer between two N-coordinated Ru^{II}/Ru^{III} redox pairs. Our interpretation of these two separate IVCT bands agrees with that of isolated trinuclear and tetranuclear CN-bridged Ru complexes.[29, 65-67] Both IVCT bands are best fit using an asymmetric peak shape, which indicates that the *as*-RuPBA fits in a transition regime of electronic delocalization according to Robin-Day classification,[68] exhibiting properties typical for both class 2 (semiconductor) and class 3 (metallic) systems, or the so-called "class 2B" system.[28] In contrast, PB belongs to the class 2A regime involving more localized charges.[68]

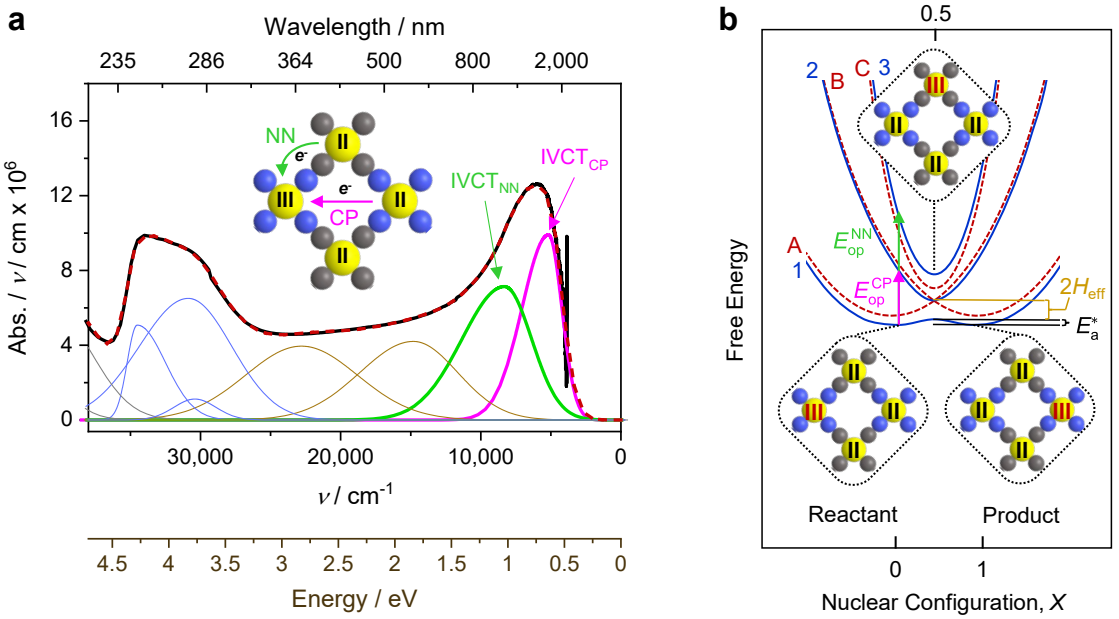

Fig. 5. Interpretation of optical charge transfer bands from UV/Vis/NIR absorption spectrum of RuPBA. **a**, Reduced absorption spectrum and fitted asymmetric gaussian peaks, highlighting two different IVCT bands for transfer between nearest neighbor cyanide bridged Ru centers ($IVCT_{NN}$) and cross-pore between N-coordinated Ru centers ($IVCT_{CP}$), as depicted in the inset scheme. The absorbance is divided by ν to accurately determine the reorganization energy and coupling in accord with theory.[28] **b**, Schematic representation for potential energy surface diagram of IVCT based on a three-state model. Red dashed lines labeled A, B, and C convey three parabolic overlapping diabatic energy surfaces, where the energy minima for A,B are equivalent and occur at $X = 0,1$. The higher energy minimum for C occurs at $X = 0.5$. Blue lines labeled 1, 2, and 3 represent the adiabatic states resulting from electronic coupling between N-coordinated donors, acceptors, and hexacyanoruthenate bridge states. The $IVCT_{CP}$ product and reactant states are of equivalent ground state energy due to symmetry. The third possible state (state 3), formed from $IVCT_{NN}$, is thermodynamically disfavored. E_{op}^{NN} and E_{op}^{CP} represent $h\nu$ for the deconvoluted peak maxima of $IVCT_{NN}$ and $IVCT_{CP}$, respectively.

The effective donor-acceptor coupling, H_{eff}, and activation energy, E_a*, were determined based on the $IVCT_{CP}$ peak energy and shape following an equivalent two-state model[28] for the three-state system depicted in Fig. 5b. The fit of the $IVCT_{CP}$ band for *as*-RuPBA gives $E_{op}^{CP} = \lambda = 0.64$ eV and a

large coupling, H_{eff} = 0.22 eV; this leads to E_a* = 16 meV, which is less than k_BT at room temperature. The $IVCT_{CP}$ rate constant, k_{ct}, is then

$$k_{ct} = \varkappa \nu_n \exp(-E_a^*/k_BT) \qquad (1)$$

where $\varkappa$ is the probability of electron transfer at the configuration coordinates (X) when the activation barrier is minimized and ν_n is a nuclear vibration frequency,[27] here assigned as the cyanide bridging ligand vibration (ca. 2130 cm^{-1}) shown in Extended Data Fig. 7, giving $\nu_n = 6.4\times10^{13}$ s^{-1}. The calculated electronic frequency[26, 69] ($\nu_{el} = 1.0\times10^{15}$ s^{-1} is much higher than ν_n, such that $\varkappa$ is essentially unity, as expected. This leads to a very fast rate constant of $k_{ct} \approx 3\times10^{13}$ s^{-1}, only slightly lower than ν_n, further supporting a Robin-Day class 2B assignment for *as*-RuPBA, but very close to class 3 delocalization.[28] The k_{ct} value corresponds to an IVCT timescale of 30 fs, which is within the sub-picosecond range measured for CT in PBAs by time-resolved spectroscopy.[70-72]

Rosseinsky and coworkers presented a simple expression for IVCT-based conductivity of PB following the treatments described by Austin-Mott and Robin-Day.[68, 73, 74] We propose a similar relationship below.

$$\sigma = pe^2d^2k_{ct}/2k_BT = ep\mu_h \qquad (2)$$

Here, the conductivity (σ) depends on the number density of hole charge carriers (p) and the distance between reactant centers (d). For $IVCT_{CP}$, the shortest distance between N-Ru centers is $d \approx 7.4$ Å based on the XRD pattern of RuPBA (Extended Data Fig. 8a). Eq. 2 also shows how k_{ct} and d relate to the hole mobility; $\mu_h = ed^2k_{ct}/2k_BT$. For *as*-RuPBA, $\mu_h \approx 4$ $cm^2/(V\cdot s)$, which is comparable to that reported for PEDOT:PSS.[75] Because both $IVCT_{CP}$ absorbance and conductivity increase as the RuPBA partially oxidizes, we propose that p must relate to the concentration of mixed valence N-Ru sites, as depicted in Fig. 5. The maximum carrier concentration occurs when the valence mixing is 1:1 II:III between N-Ru centers, corresponding to a net mixing of 3:1 II:III for all Ru centers, assuming an ideal defect-free lattice.

Closer analysis of the spectra in Fig. 4a reveals that the IVCT band manifold not only increases in absorbance, but also shifts by more than 0.3 eV to lower energy throughout the course of oxidation from *fr*-RuPBA to the most conductive mixed valence state at 1.0 V, signifying that λ and E_a* decrease while k_{ct} and μ_h increase (see Supplementary Information, Section S6). Spectroscopically determined parameters at varied E (Extended Data Table 1) indicate that mobility increases from 1 to 4 $cm^2/(V\cdot s)$ when oxidizing RuPBA over a small potential range from E = 0 to 0.1 V. However, the mobility does not vary significantly at potentials between 0.1 V and the most conductive state (E = 1.0 V), implying that the increasing carrier concentration from oxidation is the sole contributor to conductance switching in the V_{gd} range roughly between 0 and -0.5 V (Fig. 1c). The trend of increasing, constant, then decreasing mobility during partial oxidation of *fr*-RuPBA agrees well with the interpretation of the transfer curve above (Fig. 1c).

The partial density of states (pDOS) computed by DFT for different oxidation/lithiation states of RuPBA is shown in Fig. 6. The 'fully reduced,' 'partially reduced', and 'neutral' forms correspond to compositions of $Li_xRu_2[Ru(CN)_6]_2$, where x = 4, 3, and 2, respectively. The partially reduced form (*pr*-RuPBA), as depicted in Fig. 1a, is predicted to have a direct band gap of 0.50 eV, matching the experimentally determined $IVCT_{CP}$ maximum for the most conductive state. Such agreement between computed band gap and measured IVCT excitation energy was also reported for PB.[76] The fully reduced form is predicted to have a large band gap (4 eV), comparable to the energy of the observed MLCT band ($h\nu_{max} \sim 4$ eV). The calculated hole effective masses (m_h) for RuPBA range from 0.4 to 0.7; these values are similar to known semiconductors such as p-type germanium.[77] The

smallest m_h value corresponds the *pr*-RuPBA state. Based on scattering theory (see DFT Computation for details), we predict a hole charge mobility for *pr*-RuPBA of 5 $cm^2/(V \cdot s)$, which is in remarkable agreement with our experimental estimate of 4 $cm^2/(V \cdot s)$ from the MHT analysis above. The pDOS for *pr*-RuPBA reveals a delocalized electronic structure, but valence and conduction band states closest to the Fermi energy remain primarily associated with N-Ru sites. This suggests that the lowest energy excitation is between N-Ru sites, which agrees with our interpretation of the IVCT spectra (Fig. 5). Thus, both band and electron transfer theories support a mechanism whereby the electrochemically tunable degree of mixed valency between N-Ru centers directly relates to charge carrier concentration.

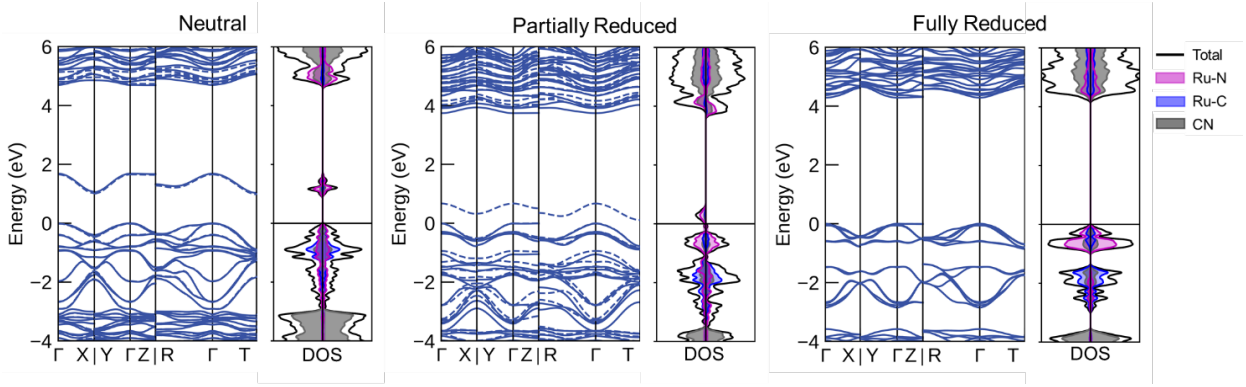

Fig. 6. DFT calculated band structures and density of states of RuPBA in the neutral, partially reduced and fully reduced states.

The m_h values for PB are larger than those of RuPBA, ranging from 1.3 to 2.9, in agreement with previously published values,[78] which is consistent with the predicted flat bands and localized states (Fig. S8), and in agreement with measurements by Long that showed RuPBA is substantially more conductive than PB.[32] The differences between PB and RuPBA band structures primarily arise from their different electron spin configurations. Unlike the high/low spin configuration of PB,[25] both N-coordinated and C-coordinated metal atoms of RuPBA are low spin, allowing for better energy alignment between neighboring Ru atoms and a more delocalized electronic structure.

The estimated mobilities presented above specifically refer to electron-hole transport within the bulk CN-bridged framework. Assuming a hole density (p) of ca. 10^{21} cm^{-3}, we estimate a bulk crystal conductivity greater than 100 S cm^{-1} for the most conductive state (*pr*-RuPBA), which is ~10,000 times greater than the measured maximum conductivity. The inkjet-printed films, however, are composed of RuPBA nanocrystals. Measurements of DC conductivity as a function of temperature for *as*-RuPBA give an activation energy of 0.18 eV, which is much higher than the activation energies estimated above from spectroscopy. CT across grain boundaries likely plays a limiting role in the observed film conductivity.[79] Importantly, this activation energy is roughly ¼ of the measured reorganization energy for the $IVCT_{CP}$ band (λ = 0.64 eV), consistent with very weak coupling and polaron hopping[74, 80] between charge-localized N-Ru centers at the interfaces between neighboring nanocrystals. We propose that electronic coupling is much weaker across grain boundaries due to the absence of NCRuCN bridges between N-coordinated Ru centers.

Towards understanding the femtosecond to nanosecond timescale dynamics governing electron transfer in RuPBA, we performed ultrafast UV/visible transient absorption spectroscopy following excitation of the metal-to-metal charge transfer transition (MMCT). These experiments used a 780 nm pump pulse to excite the MMCT transition and a white light continuum probe pulse that spanned visible wavelengths to measure the excited state UV/vis absorption at a range of time

delays following MMCT excitation. The time evolution of the UV/vis absorption can yield insights into excited state charge transfer and relaxation dynamics. For the measurements, the Au wires were not connected to a potentiostat. We performed 780 nm pump – white light probe transient absorption spectroscopy at different sample positions to attempt to disentangle the dynamics due to the electrolyte and Au wires from the dynamics specific to RuPBA. Analysis of the preliminary results showed that the 780 nm pump is exciting both the MMCT transition in RuPBA and, perhaps to a smaller extent, the plasmon resonance of the Au wires. A power dependence study of the measured spectral features yielded an unphysical 1.5-photon dependence across a wide range of 780 nm pump powers, corroborating that different excitation processes may be contributing to the observed signal. Future work will require a redesign of the specimen holder to avoid Au interference, as well as the ability to perform these measurements in the near IR to probe the IVCT dynamics.

5. SUMMARY OF EXPERIMENTAL AND COMPUTATIONAL METHODS

All reagents and solvents were purchased from Sigma-Aldrich unless otherwise noted. All water was filtered and deionized to 18.2 MΩ·cm resistivity before use (*PureLab flex* filtration system, ELGA LabWater). Custom-designed shadow masks for e-beam deposition were purchased from Stencils Unlimited, LLC.

Synthesis of RuPBA. RuPBA was synthesized following the hydrothermal method reported by Long and coworkers.[32] Ruthenium(III) acetylacetonate, $Ru(C_5H_7O_2)_3$, (0.500 g, 1.24 mmol) was added to a 20 mL aqueous solution containing 0.260 g (0.310 mmol) of potassium hexacyanoruthenate(II), $K_4[Ru(CN)_6]$. The mixture was stirred for 1 hr at room temperature and subsequently transferred to a 45-mL PTFE-lined acid digestion vessel (Parr, model 4744) and heated at 175 °C for 96 hr. The resulting black precipitate was isolated by centrifugation and washed three times with 70 mL of water. To remove $Ru(C_5H_7O_2)_3$ starting material and potential organic byproducts, the precipitate was rinsed once with 70 mL acetone, three times with 40 mL toluene, and three additional times with 40 mL acetone, using a sonication bath to redisperse the sample in each rinsing solvent and a centrifugation rate of 6000 rpm to collect the precipitate. After rinsing 5 times with 40 mL aliquots of water by sonication and centrifugation (8700 rpm), the final precipitate was redispersed in water and separated into two equal portions. The portion for XRD and elemental analysis was isolated by centrifuge and dried at 60 °C for two days before characterization. Found composition (weight %): K, 6.9; Ru, 45.7; C, 17.6; N, 15.1; H, 1.9. The second portion was isolated by centrifuge and redispersed in DMF to give a 10 mg/mL suspension for preparation of the RuPBA ink.

Preparation of RuPBA ink. Cyclohexanol (2.5 mL) was added to a 5 mL aliquot of 10 mg/mL RuPBA suspension in DMF and sonicated for 10 min. The resulting suspension was centrifuged at 2500 rpm for 5 min to collect and discard large RuPBA aggregates. The remaining suspension, ~4 mg/mL RuPBA in 2:1 DMF:cyclohexanol (v:v), was used as the RuPBA ink.

Preparation of Li ionogel ink. Lithium bis(fluorosulfonyl)imide, LiFSI, (2.035 g) was dissolved in 10 mL of 1-butyl-1-methylpyrrolidinium bis(trifluoromethanesulfonyl)imide ($Pry_{14}TFSI$) ionic liquid by stirring overnight in an Ar-filled glovebox to give a 1.0 M LiFSI in $Pry_{14}TFSI$. Preparation of the sol-gel precursor for the ionogel ink was based on the method described by Dunn and coworkers.[46] A 300 µL volume of tetraethylorthosilicate (TEOS) was added to 300 µL of triethoxyvinylsilane (TEVS) and sonicated for 15 min. While under sonication, 300 uL of formic acid was added to the TEOS/TEVS mixture and allowed to sonicate for 15 min to give the sol-gel precursor. A 550 µL aliquot of the sol-gel precursor was then added to 450 uL of the ionic liquid (1.0 M LiFSI in $Pry_{14}TFSI$) and sonicated 15 min to give a clear solution, which was subsequently diluted with 1 mL ethanol for use as the Li ionogel ink.

Preparation of protic ionogel ink. A solution containing 17.6 wt% protic ionic liquid (diethylmethylammonium trifluoromethanesulfonate, DEMA:TfO, 98%, IOLITEC), 4.4 wt% poly(vinylidene fluoride-*co*-hexafluoropropylene), and 78 wt% dimethylacetamide (DMA) was prepared by sonication and subsequently diluted by a factor of 4 with additional DMA solvent.

ECRAM device fabrication. Gold electrode patterns for ECRAM devices and Van der Pauw samples were fabricated on nanosilica-coated polyethylene terephthalate (PET) printing media (Novele™, Novacentrix) via e-beam evaporation using custom-designed shadow masks (Stencils Unlimited) by depositing 5 nm Ti adhesion layer, followed by 150 nm Au top layer. RuPBA and

ionogel layers were printed over the Au-patterned PET substrates using a Dimatix Materials Printer (DMP-2850) with DMC-11610 ink cartridges. Removable Scotch tape was used to adhere the backside of the PET substrate to an SiO_2-coated Si wafer. The fiducial camera of the DMP was used to precisely align the RuPBA prints to the Au electrode pattern array.

RuPBA films for ECRAM devices were printed using a cartridge temperature of 29 °C and substrate temperature of 55 °C. Device channels were printed with one jet nozzle at 20 μm drop spacing for optimal film quality and feature resolution, with a total of 10 print cycles. Channel films included ~75 μm of overlap with the Au contacts. For the device gates, 15 RuPBA print cycles were performed using 11 nozzles at a drop spacing of 31 μm. Two-minute rest periods were inserted in between prints for each device row to keep the cartridge temperature from exceeding 32 °C, which was found to help prevent nozzle clogging. The resulting RuPBA films were then dried at 60 °C for at least 48 hours. After realignment of the substrate, ionogel films were printed at room temperature with 20 μm drop spacing using 3 jetting nozzles and at least 6 print layers to ensure full coverage.

ECRAM devices for dopamine sensors included an additional 4 by 4 mm area to the gate to serve as the base of the reservoir for the dopamine solution. For these devices, RuPBA was printed over the entire area of Au gate electrode and the channel region, similar to the other ECRAM devices. The ionogel was printed over the region shown in Fig 3a, leaving a 4 by 4 mm RuPBA/Au region without ionogel coating. An acrylic adhesive backed plastic well was fabricated by laser cutting and attached to the device. The well was initially filled with 25 μL of 0.1 M sodium phosphate buffer, pH 5.5. A pipet was used to incrementally add 1 μL aliquots of the dopamine solution (0.1 mM dopamine hydrochloride, 0.1 M sodium phosphate buffer, pH 5.5) to the reservoir.

X-ray diffraction. Powder x-ray diffraction measurements were performed on a PANalytical Empyrean diffractometer and operated at 44 kV and 40 kA using Cu Kα radiation (λ= 1.5406 Å). A reflection-transmission spinner was used as a sample holder and the spinning rate was set at 4 rpm. The patterns were collected in the 2θ range of 5 to 75°, and the step size was 0.026°.

X-ray photoelectron spectroscopy. Samples for x-ray photoelectron spectroscopy were prepared by dropcasting the RuPBA ink on a Au-coated SiO_2/Si substrate. The spectra were acquired using Al K_α: 1486.6 eV source and monochromator (Scienta Omicron, Inc., XM 1000Mkii) under ultrahigh vacuum.

RuPBA film conductivity and ECRAM pulsed-programming measurements. Electrical measurements of Van der Pauw samples and pulsed conductance tuning of ECRAM devices were performed under N_2 atmosphere at slightly reduced pressure (~600 torr) and controlled temperature using a probe station and temperature controller (Lakeshore). Sheet resistance measurements were performed with a Keysight B1500A semiconductor device analyzer to obtain conductivity based on the measured film thickness. Current-voltage recordings were also performed at each temperature to make sure the response remained ohmic.

Pulsed programming and state retention testing of ECRAM devices was performed using a custom LabVIEW waveform generation program, as previously described,[38, 39, 81] to control analog voltage outputs and record input current to an NI-DAQ PCIe-6363 at 10 kHz sampling. To switch the ECRAM device gate to open circuit during the 'read' steps, a CMOS analog switch (MAX327, MAXIM Integrated Products) was implemented and powered by a dual output DC power supply (E3620A, Keysight). A low-noise current amplifier (FEMTO, DLPCA-200) was used to measure the current at 10^6 V/A gain and 200 kHz low-pass analog filter. The gate charge, ΔQ, resulting from trapezoidal numerical integration function in MATLAB 2019.

Cell Culture. Neuro2a cells were purchased from ATCC (CCL-131) and cultured in high-glucose DMEM (Fisher Scientific #11995073) with 10% Fetal Bovine Serum (FBS) (Seradigm Premium Grade, Avantor) and 1% Penicillin/Streptomycin (Thermo Fisher #15140122). Cells were grown at 37 °C and 5% CO_2 and passaged/harvested using Trypsin-ehylene diamine tetra acetate (Fisher Scientific #25300120).

Growth and Viability Assays. A 1 mg/mL aqueous dispersion of RuPBA was spotted onto wells of a 24-well plate (200 ul per well) and allowed to dry at room temperature for 1 hour. Cells were seeded at densities of 10,000, 25,000 and 50,000 cells/well in quadruplicate, and allowed to grow for 3 days, either in the presence or absence of RuPBA. At the end of 3 days, cells were harvested, stained with Trypan Blue (1:1 ratio, incubated for 5 minutes at room temperature) and counted using the BioRad TC20 Cell Counter. Pictures of the cells on the RuPBA substrate were taken using brightfield imaging with the EVOS M5000 imaging system (at 200× magnification).

Cells were prepared for scanning electron microscopy as previously described.[82] Briefly, cells were plated on Nunc Thermanox coverslips (Thermo Fisher #150067) and grown for 3 days in media with 10% FBS (see above). The coverslips were then fixed in 2.5% glutaraldehyde (Fisher Scientific #O2957-1) at room temperature for 30 minutes, washed 3 x 2 minutes with rinsing buffer (phosphate buffer), and post-fixed with 1% osmium tetroxide (Sigma #20816-12-0). After another 2-minute wash with rinsing buffer and 2 x 2-minute washes with deionized water, the coverslips were dried with anhydrous ethanol. Samples were then dehydrated using a CO_2 critical point dryer, sputter coated with ~1 nm Au, and imaged using a FEI Nova scanning electron microscope at 5 kV accelerating voltage.

All spectroelectrochemical measurements were performed using a BioLogic SP-300 bipotentiostat. In-situ UV-Vis-NIR spectroscopic interrogation of RuPBA films on ITO-coated glass slides (Sigma Aldrich) was performed using a JASCO V-770 spectrophotometer equipped with an integrating sphere. The spectroelectrochemical cell consisted of inkjet-printed RuPBA on ITO-coated glass (working electrode), a gold wire (counter electrode), a Ag/AgCl wire (quasireference electrode), and a quartz window in a custom-designed Teflon cell with rubber gaskets to seal electrolyte. The electrolyte contained 1.0 M LiFSI dissolved in $Pry_{14}TFSI$.

The electrochromic cell shown in the Video S1 of the Supplementary Information was constructed using two FTO-coated glass electrodes, each with inkjet-printed RuPBA films, and double-sided Kapton tape to seal the 1.0 M LiFSI in $Pry_{14}TFSI$ electrolyte between the two electrodes. The working electrode consisted of square shaped RuPBA printed film of 2.25 cm^2 area. The printed RuPBA area of the counter/reference electrode was a square frame with inner and outer square edge lengths of 3 and 4 cm (7 cm^2 frame area).

In-situ NIR absorption spectra of ECRAM devices were acquired with an NIRQuest+2.5 spectrometer from Ocean Insight. Fiber optic cables for 400-2400 nm wavelength range (Thorlabs, AFS50/125Y) were used with collimating lenses to direct the beam path of the tungsten-halogen light source through the ECRAM device using an adjustable stage for film transmission measurements (Stage-RTL-T, Ocean Insight). Blank reference measurements were performed by positioning the light beam (~0.2 mm cross-sectional diameter) at an area of the ECRAM device that included the glass microscope slide, PET substrate, and ionogel, but not RuPBA. The sample was then repositioned to pass the incident light through the middle of the RuPBA channel. Constant potentials were applied to the gate for 725 s using a BioLogic SP-300 bipotentiostat. Afterwards, the gate was set to open circuit and the channel conductance was monitored while simultaneously recording spectra (0.5 s integration time, 10 scans averaged for each spectrum).

In-situ Raman spectra were acquired with an inVia™ Raman microscope (Renishaw) using a 633 nm laser at 0.1% power. Using a 50X objective, the beam was focused to an area where the RuPBA channel film coats one of the Au contacts. The plasmonic enhancement from Au was found to be necessary to achieve sufficient signal. Acquisition settings: 50 s exposure time, 60 accumulations (3000 s total acquisition time per spectrum).

DFT Computation All density functional theory calculations were performed using the Vienna ab initio simulation package (VASP).[83] The geometry and electronic properties were predicted using the hybrid HSE06 exchange-correlation functional within the spin polarization formulism. The planewave basis set energy cut-off was set to 500 eV and a 3x3x2 k-point grid was using during geometry optimization (atomic positions and cell volume). The geometries were optimized until all forces were below 0.02 eV/Å. A single-point calculation was then preformed, with a k-point grid of 6x6x4, to determine the density of states. The band structures and hole effective masses (m_h) were determined using AMSET[84] which depends on BoltzTrap2[85] for interpolation. Seekpath[86] was used to determine the high symmetry band paths; note, some paths have been omitted in Figures 6 and S9 for aesthetics reasons because they looked visually similar. The lowest m_h determine via AMSET at gamma are reported. Three oxidization states were considered for both PB and RuPBA; fully reduced (*fr*), partially reduced (*pr*), and neutral. The different oxidization states were achieved by varying the number of Li atoms (4, 3 and 2 Li atoms respectively; note, PB calculations were performed with K in place of Li). An orthorhombic unit cell was used containing 4 Ru (see Fig. S7 of Supplementary Information) which is the smallest system allowing for a *pr* state to be represented.

The hole charge mobility was calculated for *pr*-RuPBA with the PBEsol+U functional using a Hubbard U_{eff} value of 4.0 eV (resulting band gap is in good agreement with HSE06). The planewave basis set energy cut-off was set to 500 eV and a 4x4x3 k-point grid was used during geometry optimization; the geometry was relaxed until all forces were less 0.0005 eV/Å. The elastic constants, effective phonon frequency, static and high-frequency dielectric constants and deformation potential were calculated at the same level on theory. A signal-point calculation using a denser k-point mesh, 8x8x6, was used to obtain the wave function coefficients and for band structure interpolation. These properties/calculations were used to determine acoustic deformation, ionized impurity, and polar optical phonon scattering. The reported hole mobility is calculated for a carrier concentration of $1.8x10^{21}$ cm^{-3} which corresponds to 1 carrier per unit volume. The charge mobility calculation was performed using AMSET[84].

6. CONCLUSIONS AND OUTLOOK

We have shown that the class of active materials for electrochemical transistors extends well beyond extensively studied organic polymers and transition metal chalcogenides into the realm of extended coordination frameworks like RuPBA. Our findings open a window to study electrochemically tunable conductivity in related mixed valence coordination structures such as other PBAs, coordination polymers, and metal-organic frameworks. Two different theoretical approaches, electron transfer theory and Boltzmann transport theory, independently predict similar carrier mobilities within the RuPBA bulk. Our spectroscopic analysis emphasizes that the Marcus-Hush model is not only applicable to CT kinetics in small molecules, but also provides physical insight into mixed valence conductors that belong to the Robin-Day class 2-3 transition regime,[28, 68] exhibiting characteristics of both intervalence hopping and band-like transport due to an intermediate degree of electron delocalization. Both theoretical treatments also support the proposed $IVCT_{CP}$ transport pathway. We anticipate major improvements to ECRAM and other electronic applications as devices are made smaller and look forward to taking advantage of RuPBA's sensitivity to neurotransmitters to achieve communication between biological and artificial neurons.

REFERENCES

[1] Li, Y. B.; Wang, Z. R.; Midya, R.; Xia, Q. F.; Yang, J. J., Review of memristor devices in neuromorphic computing: materials sciences and device challenges. *Journal of Physics D-Applied Physics* **2018,** *51*, 50.
[2] Zhu, J. D.; Zhang, T.; Yang, Y. C.; Huang, R., A comprehensive review on emerging artificial neuromorphic devices. *Applied Physics Reviews* **2020,** *7*, 1.
[3] Fuller, E. J.; Keene, S. T.; Melianas, A.; Wang, Z. R.; Agarwal, S.; Li, Y. Y.; Tuchman, Y.; James, C. D.; Marinella, M. J.; Yang, J. J.; Salleo, A.; Talin, A. A., Parallel programming of an ionic floating-gate memory array for scalable neuromorphic computing. *Science* **2019,** *364*, 570.
[4] Agarwal, S.; Plimpton, S. J.; Hughart, D. R.; Hsia, A. H.; Richter, I.; Cox, J. A.; James, C. D.; Marinella, M. J. In *Resistive memory device requirements for a neural algorithm accelerator*, 2016 International Joint Conference on Neural Networks (IJCNN), 24-29 July 2016; 929.
[5] Islam, R.; Li, H. T.; Chen, P. Y.; Wan, W. E.; Chen, H. Y.; Gao, B.; Wu, H. Q.; Yu, S. M.; Saraswat, K.; Wong, H. S. P., Device and materials requirements for neuromorphic computing. *Journal of Physics D-Applied Physics* **2019,** *52*, 1.
[6] Rivnay, J.; Inal, S.; Salleo, A.; Owens, R. M.; Berggren, M.; Malliaras, G. G., Organic electrochemical transistors. *Nature Reviews Materials* **2018,** *3*, 17086.
[7] Sood, A.; Poletayev, A. D.; Cogswell, D. A.; Csernica, P. M.; Mefford, J. T.; Fraggedakis, D.; Toney, M. F.; Lindenberg, A. M.; Bazant, M. Z.; Chueh, W. C., Electrochemical ion insertion from the atomic to the device scale. *Nature Reviews Materials* **2021,** *6*, 847.
[8] Keggin, J. F.; Miles, F. D., Structures and Formulæ of the Prussian Blues and Related Compounds. *Nature* **1936,** *137*, 577.
[9] Simonov, A.; De Baerdemaeker, T.; Boström, H. L. B.; Ríos Gómez, M. L.; Gray, H. J.; Chernyshov, D.; Bosak, A.; Bürgi, H.-B.; Goodwin, A. L., Hidden diversity of vacancy networks in Prussian blue analogues. *Nature* **2020,** *578*, 256.
[10] Avila, Y.; Acevedo-Peña, P.; Reguera, L.; Reguera, E., Recent progress in transition metal hexacyanometallates: From structure to properties and functionality. *Coord. Chem. Rev.* **2022,** *453*, 214274.
[11] Song, X.; Song, S.; Wang, D.; Zhang, H., Prussian Blue Analogs and Their Derived Nanomaterials for Electrochemical Energy Storage and Electrocatalysis. *Small Methods* **2021,** *5*, 2001000.
[12] Yi, H.; Qin, R.; Ding, S.; Wang, Y.; Li, S.; Zhao, Q.; Pan, F., Structure and Properties of Prussian Blue Analogues in Energy Storage and Conversion Applications. *Adv. Funct. Mater.* **2021,** *31*, 2006970.
[13] Zhou, A.; Cheng, W.; Wang, W.; Zhao, Q.; Xie, J.; Zhang, W.; Gao, H.; Xue, L.; Li, J., Hexacyanoferrate-Type Prussian Blue Analogs: Principles and Advances Toward High-Performance Sodium and Potassium Ion Batteries. *Advanced Energy Materials* **2021,** *11* (2), 2000943.
[14] Wu, X.; Hong, J. J.; Shin, W.; Ma, L.; Liu, T.; Bi, X.; Yuan, Y.; Qi, Y.; Surta, T. W.; Huang, W.; Neuefeind, J.; Wu, T.; Greaney, P. A.; Lu, J.; Ji, X., Diffusion-free Grotthuss topochemistry for high-rate and long-life proton batteries. *Nat. Energy* **2019,** *4* (2), 123-130.
[15] Ono, K.; Ishizaki, M.; Kanaizuka, K.; Togashi, T.; Yamada, T.; Kitagawa, H.; Kurihara, M., Grain-Boundary-Free Super-Proton Conduction of a Solution-Processed Prussian-Blue Nanoparticle Film. *Angew. Chem. Int. Ed.* **2017,** *56* (20), 5531-5535.
[16] Pearce, J., Studies of any toxicological effects of Prussian blue compounds in mammals—A review. *Food Chem. Toxicol.* **1994,** *32*, 577.

[17] Kong, B.; Selomulya, C.; Zheng, G.; Zhao, D., New faces of porous Prussian blue: interfacial assembly of integrated hetero-structures for sensing applications. *Chem. Soc. Rev.* **2015,** *44*, 7997-8018.
[18] Cobo, S.; Molnár, G.; Carcenac, F.; Szilágyi, P. A.; Salmon, L.; Vieu, C.; Bousseksou, A., Thin films of Prussian blue: sequential assembly, patterning and electron transport properties at the nanometric scale. *J Nanosci Nanotechnol* **2010,** *10*, 5042-50.
[19] Song, Y. Y.; Jia, W.-Z.; Li, Y.; Xia, X.-H.; Wang, Q.-J.; Zhao, J.-W.; Yan, Y.-D., Synthesis and Patterning of Prussian Blue Nanostructures on Silicon Wafer via Galvanic Displacement Reaction. *Adv. Funct. Mater.* **2007,** *17*, 2808-2814.
[20] Manumpil, M. A.; Leal-Cervantes, C.; Hudson, M. R.; Brown, C. M.; Karunadasa, H. I., Electronic Conductivity in a Porous Vanadyl Prussian Blue Analogue upon Air Exposure. *Inorg. Chem.* **2017,** *56*, 12682-12686.
[21] Hosseini, P.; Wolkersdörfer, K.; Wark, M.; Redel, E.; Baumgart, H.; Wittstock, G., Morphology and Conductivity of Copper Hexacyanoferrate Films. *The Journal of Physical Chemistry C* **2020,** *124* (31), 16849-16859.
[22] Tennakone, K.; Dharmaratne, W. G. D., Experimental and theoretical study of electronic conduction in H_2O-doped Prussian blue. *Journal of Physics C: Solid State Physics* **1983,** *16*, 5633-5639.
[23] Rosseinsky, D. R.; Tonge, J. S.; Berthelot, J.; Cassidy, J. F., Site-transfer conductivity in solid iron hexacyanoferrates by dielectric relaxometry, voltammetry and spectroscopy. Prussian Blue, congeners and mixtures. *Journal of the Chemical Society, Faraday Transactions 1: Physical Chemistry in Condensed Phases* **1987,** *83*, 231-243.
[24] Xidis, A.; Neff, V. D., On the Electronic Conduction in Dry Thin Films of Prussian Blue, Prussian Yellow, and Everitt's Salt. *J. Electrochem. Soc.* **1991,** *138*, 3637-3642.
[25] Pajerowski, D. M.; Watanabe, T.; Yamamoto, T.; Einaga, Y., Electronic conductivity in Berlin green and Prussian blue. *Physical Review B* **2011,** *83*, 153202.
[26] Piechota, E. J.; Meyer, G. J., Introduction to Electron Transfer: Theoretical Foundations and Pedagogical Examples. *J. Chem. Educ.* **2019,** *96*, 2450-2466.
[27] Demadis, K. D.; Hartshorn, C. M.; Meyer, T. J., The Localized-to-Delocalized Transition in Mixed-Valence Chemistry. *Chem. Rev.* **2001,** *101* (9), 2655-2686.
[28] Brunschwig, B. S.; Creutz, C.; Sutin, N., Optical transitions of symmetrical mixed-valence systems in the Class II–III transition regime. *Chem. Soc. Rev.* **2002,** *31* (3), 168-184.
[29] D'Alessandro, D. M.; Keene, F. R., Intervalence Charge Transfer (IVCT) in Trinuclear and Tetranuclear Complexes of Iron, Ruthenium, and Osmium. *Chem. Rev.* **2006,** *106* (6), 2270-2298.
[30] Murase, R.; Leong, C. F.; D'Alessandro, D. M., Mixed Valency as a Strategy for Achieving Charge Delocalization in Semiconducting and Conducting Framework Materials. *Inorg. Chem.* **2017,** *56*, 14373-14382.
[31] Shatruk, M.; Dragulescu-Andrasi, A.; Chambers, K. E.; Stoian, S. A.; Bominaar, E. L.; Achim, C.; Dunbar, K. R., Properties of Prussian Blue Materials Manifested in Molecular Complexes: Observation of Cyanide Linkage Isomerism and Spin-Crossover Behavior in Pentanuclear Cyanide Clusters. *Journal of the American Chemical Society* **2007,** *129* (19), 6104-6116.
[32] Behera, J. N.; D'Alessandro, D. M.; Soheilnia, N.; Long, J. R., Synthesis and Characterization of Ruthenium and Iron−Ruthenium Prussian Blue Analogues. *Chem. Mater.* **2009,** *21* (9), 1922-1926.
[33] Talin, A. A.; Centrone, A.; Ford, A. C.; Foster, M. E.; Stavila, V.; Haney, P.; Kinney, R. A.; Szalai, V.; Gabaly, F. E.; Yoon, H. P.; Léonard, F.; Allendorf, M. D., Tunable Electrical Conductivity in Metal-Organic Framework Thin-Film Devices. *Science* **2014,** *343*, 66-69.
[34] Aubrey, M. L.; Wiers, B. M.; Andrews, S. C.; Sakurai, T.; Reyes-Lillo, S. E.; Hamed, S. M.; Yu, C.-J.; Darago, L. E.; Mason, J. A.; Baeg, J.-O.; Grandjean, F.; Long, G. J.; Seki, S.; Neaton, J.

B.; Yang, P.; Long, J. R., Electron delocalization and charge mobility as a function of reduction in a metal–organic framework. *Nat. Mater.* **2018,** *17*, 625-632.
[35] Van de Burgt, Y.; Melianas, A.; Keene, S. T.; Malliaras, G.; Salleo, A., Organic electronics for neuromorphic computing. *Nature Electronics* **2018,** *1*, 386-397.
[36] Rivnay, J.; Inal, S.; Salleo, A.; Owens, R. M.; Berggren, M.; Malliaras, G. G., Organic electrochemical transistors. *Nature Reviews Materials* **2018,** *3*, 17086.
[37] Van de Burgt, Y.; Lubberman, E.; Fuller, E. J.; Keene, S. T.; Faria, G. C.; Agarwal, S.; Marinella, M. J.; Alec Talin, A.; Salleo, A., A non-volatile organic electrochemical device as a low-voltage artificial synapse for neuromorphic computing. *Nat. Mater.* **2017,** *16*, 414-418.
[38] Fuller, E. J.; Keene, S. T.; Melianas, A.; Wang, Z.; Agarwal, S.; Li, Y.; Tuchman, Y.; James, C. D.; Marinella, M. J.; Yang, J. J.; Salleo, A.; Talin, A. A., Parallel programming of an ionic floating-gate memory array for scalable neuromorphic computing. *Science* **2019,** *364*, 570-574.
[39] Li, Y.; Xiao, T. P.; Bennett, C. H.; Isele, E.; Melianas, A.; Tao, H.; Marinella, M. J.; Salleo, A.; Fuller, E. J.; Talin, A. A., In situ Parallel Training of Analog Neural Network Using Electrochemical Random-Access Memory. *Front Neurosci* **2021,** *15*, 636127-636127.
[40] Keene, S. T.; Lubrano, C.; Kazemzadeh, S.; Melianas, A.; Tuchman, Y.; Polino, G.; Scognamiglio, P.; Cinà, L.; Salleo, A.; van de Burgt, Y.; Santoro, F., A biohybrid synapse with neurotransmitter-mediated plasticity. *Nat. Mater.* **2020,** *19*, 969-973.
[41] Marcus, R. A., On the Theory of Oxidation-Reduction Reactions Involving Electron Transfer. I. *The Journal of Chemical Physics* **1956,** *24*, 966-978.
[42] Hush, N. S., Adiabatic theory of outer sphere electron-transfer reactions in solution. *Transactions of the Faraday Society* **1961,** *57* (0), 557-580.
[43] Fuller, E. J.; Gabaly, F. E.; Léonard, F.; Agarwal, S.; Plimpton, S. J.; Jacobs-Gedrim, R. B.; James, C. D.; Marinella, M. J.; Talin, A. A., Li-Ion Synaptic Transistor for Low Power Analog Computing. *Adv. Mater.* **2017,** *29* (4), 1604310.
[44] Tang, J.; Bishop, D.; Kim, S.; Copel, M.; Gokmen, T.; Todorov, T.; Shin, S.; Lee, K. T.; Solomon, P.; Chan, K.; Haensch, W.; Rozen, J. In *ECRAM as Scalable Synaptic Cell for High-Speed, Low-Power Neuromorphic Computing*, 2018 IEEE International Electron Devices Meeting (IEDM), 1-5 Dec. 2018; 2018; pp 13.1.1-13.1.4.
[45] Ishizaki, M.; Ando, H.; Yamada, N.; Tsumoto, K.; Ono, K.; Sutoh, H.; Nakamura, T.; Nakao, Y.; Kurihara, M., Redox-coupled alkali-metal ion transport mechanism in binder-free films of Prussian blue nanoparticles. *Journal of Materials Chemistry A* **2019,** *7* (9), 4777-4787.
[46] Ashby, D. S.; DeBlock, R. H.; Lai, C.-H.; Choi, C. S.; Dunn, B. S., Patternable, Solution-Processed Ionogels for Thin-Film Lithium-Ion Electrolytes. *Joule* **2017,** *1* (2), 344-358.
[47] Keene, S. T.; Melianas, A.; van de Burgt, Y.; Salleo, A., Mechanisms for Enhanced State Retention and Stability in Redox-Gated Organic Neuromorphic Devices. *Adv. Electron. Mater.* **2019,** *5*, 1800686.
[48] Melianas, A.; Quill, T. J.; LeCroy, G.; Tuchman, Y.; Loo, H. v.; Keene, S. T.; Giovannitti, A.; Lee, H. R.; Maria, I. P.; McCulloch, I.; Salleo, A., Temperature-resilient solid-state organic artificial synapses for neuromorphic computing. *Sci. Adv.* **2020,** *6* (27), eabb2958.
[49] Xiao, T. P.; Bennett, C. H.; Feinberg, B.; Agarwal, S.; Marinella, M. J., Analog architectures for neural network acceleration based on non-volatile memory. *Applied Physics Reviews* **2020,** *7* (3), 031301.
[50] Xiang, Y.; Huang, P.; Zhao, Y.; Zhao, M.; Gao, B.; Wu, H.; Qian, H.; Liu, X.; Kang, J., Impacts of State Instability and Retention Failure of Filamentary Analog RRAM on the Performance of Deep Neural Network. *IEEE Transactions on Electron Devices* **2019,** *66*, 4517-4522.

[51] Xiao, T. P.; Feinberg, B.; Bennett, C. H.; Prabhakar, V.; Saxena, P.; Agrawal, V.; Agarwal, S.; Marinella, M. J., On the accuracy of analog neural network inference accelerators. *arXiv preprint arXiv:2109.01262* **2021**.
[52] Yu, S., Neuro-inspired computing with emerging nonvolatile memorys. *Proceedings of the IEEE* **2018,** *106*, 260-285.
[53] Marinella, M. J.; Agarwal, S.; Hsia, A.; Richter, I.; Jacobs-Gedrim, R.; Niroula, J.; Plimpton, S. J.; Ipek, E.; James, C. D., Multiscale Co-Design Analysis of Energy, Latency, Area, and Accuracy of a ReRAM Analog Neural Training Accelerator. *IEEE Journal on Emerging and Selected Topics in Circuits and Systems* **2018,** *8*, 86-101.
[54] Zhang, C.; Zhou, P. In *A Quantized Training Framework for Robust and Accurate ReRAM-based Neural Network Accelerators*, 2021 26th Asia and South Pacific Design Automation Conference (ASP-DAC), 18-21 Jan. 2021; 2021; pp 43-48.
[55] Duda, R. O.; Hart, P. E., *Pattern classification and scene analysis*. Wiley New York: 1973; Vol. 3.
[56] Garris, M. D.; Blue, J. L.; Candela, G. T., NIST form-based handprint recognition system (release 2.0). **1997**.
[57] Candela, M. G. J. B. G.; Grother, D. D. J. G. P.; Janet, S.; Wilson, C. *NIST form-based handprint recognition system*; Technical Report NISTIR 5469, Nat'l Inst. of Standards and Technology: 1994.
[58] Xiao, H.; Rasul, K.; Vollgraf, R., Fashion-mnist: a novel image dataset for benchmarking machine learning algorithms. *arXiv preprint arXiv:1708.07747* **2017**.
[59] LeCun, Y.; Bottou, L.; Bengio, Y.; Haffner, P., Gradient-based learning applied to document recognition. *Proceedings of the IEEE* **1998,** *86* (11), 2278-2324.
[60] Fuller, E. J.; Li, Y.; Bennet, C.; Keene, S. T.; Melianas, A.; Agarwal, S.; Marinella, M. J.; Salleo, A.; Talin, A. A., Redox transistors for neuromorphic computing. *IBM Journal of Research and Development* **2019,** *63* (6), 9:1-9:9.
[61] Li, Y.; Fuller, E. J.; Sugar, J. D.; Yoo, S.; Ashby, D. S.; Bennett, C. H.; Horton, R. D.; Bartsch, M. S.; Marinella, M. J.; Lu, W. D.; Talin, A. A., Filament-Free Bulk Resistive Memory Enables Deterministic Analogue Switching. *Adv. Mater.* **2020,** *32*, 2003984.
[62] Agarwal, S.; Garland, D.; Niroula, J.; Jacobs-Gedrim, R. B.; Hsia, A.; Heukelom, M. S. V.; Fuller, E.; Draper, B.; Marinella, M. J., Using Floating-Gate Memory to Train Ideal Accuracy Neural Networks. *IEEE Journal on Exploratory Solid-State Computational Devices and Circuits* **2019,** *5*, 52-57.
[63] Kuzum, D.; Yu, S.; Philip Wong, H. S., Synaptic electronics: materials, devices and applications. *Nanotechnology* **2013,** *24*, 382001.
[64] Gualandi, I.; Tonelli, D.; Mariani, F.; Scavetta, E.; Marzocchi, M.; Fraboni, B., Selective detection of dopamine with an all PEDOT: PSS organic electrochemical transistor. *Scientific reports* **2016,** *6*, 1-10.
[65] Bignozzi, C. A.; Roffia, S.; Scandola, F., Intervalence transfer in cyano-bridged bi- and trinuclear ruthenium complexes. *Journal of the American Chemical Society* **1985,** *107*, 1644-1651.
[66] Pieslinger, G. E.; Albores, P.; Slep, L. D.; Coe, B. J.; Timpson, C. J.; Baraldo, L. M., Communication between Remote Moieties in Linear Ru–Ru–Ru Trimetallic Cyanide-Bridged Complexes. *Inorg. Chem.* **2013,** *52*, 2906-2917.
[67] Lin, J.-L.; Tsai, C.-N.; Huang, S.-Y.; Endicott, J. F.; Chen, Y.-J.; Chen, H.-Y., Nearest- and Next-Nearest-Neighbor Ru(II)/Ru(III) Electronic Coupling in Cyanide-Bridged Tetra-Ruthenium Square Complexes. *Inorg. Chem.* **2011,** *50*, 8274-8280.
[68] Robin, M. B.; Day, P., Mixed Valence Chemistry-A Survey and Classification. In *Advances in Inorganic Chemistry and Radiochemistry*, Emeléus, H. J.; Sharpe, A. G., Eds. Academic Press: 1968; Vol. 10, pp 247-422.
[69] Newton, M. D., Quantum chemical probes of electron-transfer kinetics: the nature of donor-acceptor interactions. *Chem. Rev.* **1991,** *91*, 767-792.

[70] Arnett, D. C.; Voehringer, P.; Scherer, N. F., Excitation Dephasing, Product Formation, and Vibrational Coherence in an Intervalence Charge-Transfer Reaction. *Journal of the American Chemical Society* **1995,** *117*, 12262-12272.
[71] Cammarata, M.; Zerdane, S.; Balducci, L.; Azzolina, G.; Mazerat, S.; Exertier, C.; Trabuco, M.; Levantino, M.; Alonso-Mori, R.; Glownia, J. M.; Song, S.; Catala, L.; Mallah, T.; Matar, S. F.; Collet, E., Charge transfer driven by ultrafast spin transition in a CoFe Prussian blue analogue. *Nature Chemistry* **2021,** *13* (1), 10-14.
[72] Barlow, K.; Johansson, J. O., Ultrafast photoinduced dynamics in Prussian blue analogues. *Phys. Chem. Chem. Phys.* **2021,** *23* (14), 8118-8131.
[73] England, S. J.; Kathirgamanathan, P.; Rosseinsky, D. R., Perturbation calculation from the charge-transfer spectrum data of intervalence site-transfer D.C. conductivity in Prussian Blue *Chem. Commun.* **1980**, 840-841.
[74] Austin, I. G.; Mott, N. F., Polarons in crystalline and non-crystalline materials. *Advances in Physics* **1969,** *18*, 41-102.
[75] Wei, Q.; Mukaida, M.; Naitoh, Y.; Ishida, T., Morphological Change and Mobility Enhancement in PEDOT:PSS by Adding Co-solvents. *Adv. Mater.* **2013,** *25*, 2831-2836.
[76] Wojdeł, J. C.; Moreira, I. d. P. R.; Bromley, S. T.; Illas, F., On the prediction of the crystal and electronic structure of mixed-valence materials by periodic density functional calculations: The case of Prussian Blue. *The Journal of Chemical Physics* **2008,** *128*, 044713.
[77] Spitzer, W. G.; Fan, H. Y., Determination of Optical Constants and Carrier Effective Mass of Semiconductors. *Physical Review* **1957,** *106* (5), 882-890.
[78] Hurlbutt, K.; Giustino, F.; Pasta, M.; Volonakis, G., Electronic Structure and Electron-Transport Properties of Three Metal Hexacyanoferrates. *Chem. Mater.* **2021,** *33* (17), 7067-7074.
[79] Foster, M. E.; Sohlberg, K.; Allendorf, M. D.; Talin, A. A., Unraveling the Semiconducting/Metallic Discrepancy in Ni3(HITP)2. *The Journal of Physical Chemistry Letters* **2018,** *9*, 481-486.
[80] Furutsuki, S.; Chung, S.-C.; Nishimura, S.-i.; Kudo, Y.; Yamashita, K.; Yamada, A., Electrochromism of Li_xFePO_4 Induced by Intervalence Charge Transfer Transition. *The Journal of Physical Chemistry C* **2012,** *11*, 15259-15264.
[81] Li, Y.; Fuller, E. J.; Asapu, S.; Agarwal, S.; Kurita, T.; Yang, J. J.; Talin, A. A., Low-Voltage, CMOS-Free Synaptic Memory Based on LiXTiO2 Redox Transistors. *ACS Applied Materials & Interfaces* **2019,** *11*, 38982-38992.
[82] Fischer, E. R.; Hansen, B. T.; Nair, V.; Hoyt, F. H.; Dorward, D. W., Scanning electron microscopy. *Curr Protoc Microbiol* **2012,** *Chapter 2*, Unit2B.2-2B.2.
[83] Kresse, G.; Furthmüller, J., Efficient iterative schemes for ab initio total-energy calculations using a plane-wave basis set. *Physical review B* **1996,** *54* (16), 11169.
[84] Ganose, A. M.; Park, J.; Faghaninia, A.; Woods-Robinson, R.; Persson, K. A.; Jain, A., Efficient calculation of carrier scattering rates from first principles. *Nature Communications* **2021,** *12*, 2222.
[85] Madsen, G. K. H.; Carrete, J.; Verstraete, M. J., BoltzTraP2, a program for interpolating band structures and calculating semi-classical transport coefficients. *Comput. Phys. Commun.* **2018,** *231*, 140-145.
[86] Hinuma, Y.; Pizzi, G.; Kumagai, Y.; Oba, F.; Tanaka, I., Band structure diagram paths based on crystallography. *Computational Materials Science* **2017,** *128*, 140-184.

DISTRIBUTION

Email—Internal

Name	Org.	Sandia Email Address
A. Talin	8342	aatalin@sandia.gov
M. Allendorf	8300	mdallen@sandia.gov
D. Robinson	8342	darobin@sandia.gov
K. Ramasesha	8352	kramase@sandia.gov
E. J. Fuller	8342	ejfull@sandia.gov
A. Bhandarkar	8342	abhanda@sandia.gov
V. Stavila	8341	vnstavi@sandia.gov
R. Krishnakumar	8623	rkrishn@sandia.gov
M. Marinella	5252	mmarine@sandia.gov
C. Bennett	5252	cbennet@sandia.gov
C. Spataru	8342	cdspata@sandia.gov
A. Huq	8342	ahuq@sandia.gov
C. Gutierrez	1870	cgutie@sandia.gov
C. Mailhiot	8340	cmailhi@sandia.gov
Technical Library	01911	sanddocs@sandia.gov

This page left blank

This page left blank

Sandia National Laboratories

Sandia National Laboratories is a multimission laboratory managed and operated by National Technology & Engineering Solutions of Sandia LLC, a wholly owned subsidiary of Honeywell International Inc. for the U.S. Department of Energy's National Nuclear Security Administration under contract DE-NA0003525.